Realization of an intense cold Rb atomic beam based on a two-dimensional magneto-optical trap: Experiments and comparison with simulations

Saptarishi Chaudhuri,* Sanjukta Roy,† and C. S. Unnikrishnan‡
Fundamental Interactions Laboratory, Gravitation Group, Tata Institute of Fundamental Research, Mumbai-400005, India
(Received 6 April 2006; published 18 August 2006)

We discuss the implementation and characterization of the source of a slow, intense, and collimated beam of rubidium atoms. The cold atomic beam is produced by two-dimensional magneto-optical trapping in directions transverse to the atomic beam axis and unbalanced Doppler cooling in the axial direction. The vacuum design allows use of relatively low laser power and a considerably simplified assembly. The atomic beam has a high flux of about 2×10^{10} atoms/s at a total cooling laser power of 55 mW. It has a narrow longitudinal velocity distribution with mean velocity 15 m/s with full width at half maximum 3.5 m/s and has a low divergence of 26 mrad. The high flux enables ultrafast loading of about 10^{10} atoms into a three-dimensional (3D) magneto-optical trap within 500 ms. The variation of the atomic beam flux was studied as a function of the rubidium vapor pressure, cooling laser power, transverse cooling laser beam length, detuning of the cooling laser, and relative intensities of the cooling beams along the atomic beam axis. We also discuss a detailed comparison of our measurements of the cold atomic beam with a 3D numerical simulation.

DOI: 10.1103/PhysRevA.74.023406 PACS number(s): 32.80.Pj, 39.10.+j

I. INTRODUCTION

Cold atomic beams are of increasing significance in a variety of experiments and applications such as atom optics [1], atom interferometry [2], the study of cavity QED effects [3], atom lasers [4], the production of Bose-Einstein condensation, etc. The desirable features for cold beams of neutral atoms are high flux at low average velocity, small divergence, tunability of flux and velocity, and robustness and stability in the beam parameters.

In order to produce a large BEC and an atom laser, a high initial atom number in a magneto-optical trap (MOT) is essential as a starting point for evaporative cooling so that there would be enough atoms remaining even after the losses during evaporative cooling. Loading a MOT from the background thermal atoms using a getter source is a simple and convenient way to produce cold atomic samples but this procedure does not produce a high equilibrium atom number. Typically, such traps produce clouds containing less than 10^8 atoms when the background vapor pressure is about 10^{-9} mbar, that too in a loading time of about 10 s. The conflicting requirements of UHV below 10^{-10} mbar for magnetic trap BEC's and the need to have a large number of atoms in the trap are usually resolved by a double-MOT arrangement or its variations, set up in two vacuum chambers with a differential pumping port in between. More recently, the advantages of the more compact and efficient arrangement with two-dimensional (2D) magneto-optical trapping are recognized. A high number of atoms can be loaded very fast into a 3D MOT if loaded from a continuous source of a cold atomic beam with high flux.

There has been remarkable progress in the recent past in producing high-flux, low-velocity atomic beams for various applications. Zeeman slowers [5] are still widely used to obtain a high flux of atoms (about 10^{11} atoms/s) by deceleration of a thermal atomic beam along its propagation axis using radiation pressure. Zeeman slowers give a high flux of atoms at the expense of a relatively large divergence of the atomic beam. The recent trend is to generate the atomic beam from a magneto-optical trap itself, operated at a higher vapor pressure, without a Zeeman slower. A low-velocity intense source (LVIS) [6] was realized by Lu *et al.* with narrow longitudinal velocity distribution with mean velocity 14 m/s and flux of 5×10^9 atoms/s by creating a narrow dark column at the center of one of the six MOT laser beams. A pure 2D MOT was realized by Schoser *et al.* [7] where a 2D quadrupole magnetic field was used with transverse optical cooling along the two axes orthogonal to the atomic beam. A high flux of 6×10^{10} atoms/s was obtained with mean longitudinal velocity of 50 m/s, using a high laser power of 160 mW per beam for cooling. A configuration in which two-dimensional magneto-optical trapping is complemented with a pair of laser beams in the axial direction for optical molasses cooling is referred to as a $2D^+$ MOT. A $2D^+$ MOT source of cold atoms with a flux of 9×10^9 atoms/s at a mean velocity of 8 m/s was produced by Dieckmann *et al.* [8]. A similar approach was used by Conroy *et al.* [9] to produce a source of cold atoms for loading into a magnetic guide. To further narrow the longitudinal velocity distribution, two-dimensional magneto-optical trapping along with cooling by a moving molasses along the third direction was done by Cren *et al.* [10]. A cold atomic beam can also be produced by extracting a continuous jet of cold atoms from a magneto-optical trap using a thin laser beam [11] or from a pyramidal magneto-optic trap [12]. A dual 2D MOT that serves as the source for a double-beam matter interferometry device has been completed recently at the University of Hannover [2]. The choice of the method for producing the cold atomic beam depends on the specific requirements of the subsequent experiment.

A survey of different experimental setups has motivated us to make a new design for a $2D^+$ MOT source in which a

*Electronic address: wrishi@tifr.res.in
†Electronic address: sanjukta@tifr.res.in
‡Electronic address: unni@tifr.res.in

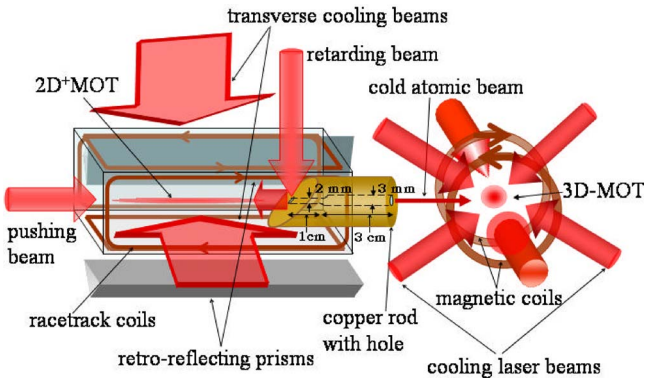

FIG. 1. (Color online) The schematic diagram of the experimental arrangement to produce cold atomic beam which loads atoms into a 3D MOT.

cold atomic beam with flux of about 2×10^{10} atoms/s with mean longitudinal velocity of 15 m/s could be produced using a total laser power less than 55 mW at relatively low rubidium vapor pressure in the $2D^+$ MOT chamber. Remarkably, when the beam parameters are well optimized, we are able to load a 3D MOT with a large number of atoms (1.2×10^{10}) in less than 500 ms. This ultrafast loading rate of about 2×10^7 atoms/ms is several thousand times faster than the MOT loading rate in a single-UHV-chamber getter-based system, and it is about 100 times faster than in typical double-MOT systems. Our setup has the added advantage of the simplest design of the $2D^+$ MOT vacuum chamber with double-sided antireflection- (AR-) coated windows and of the optics configuration for the 2D cooling. In subsequent sections, we describe our experimental setup, its aspects, the measurements used for the diagnostics of the atomic beam, the details of the 3D numerical simulation to model the atomic beam characteristics, and the comparison between the experimental and simulation results.

II. EXPERIMENTAL SETUP

The primary focus in the design of our $2D^+$ MOT source [8] was the production of an intense cold atomic beam using relatively low laser power and low Rb vapor pressure in a vacuum chamber that allows simple and reliable assembly of large AR-coated optical windows. It is desirable to have a vacuum design in which one could use easily replaceable double-sided AR-coated glass windows so as to enable retroreflection of the cooling laser beams without appreciable power imbalance or loss. Also, avoiding UHV glues or metal seals increases reliability and considerably improves the ease of implementation compared to many earlier designs of such sources. The experimental setup consists of a two-chamber vacuum system connected through a differential pumping hole as shown in Fig. 1. One is a cuboid chamber of size 16.4 cm×4 cm×4 cm, operating in the vacuum range 3×10^{-8}–1×10^{-6} mbar, in which the $2D^+$ MOT is produced. The other is a multiport spherical square UHV chamber (Kimball Physics) where the 3D MOT is produced with the atoms captured from the cold atomic beam from the $2D^+$ MOT source. The atomic beam passes to the UHV chamber through the differential pumping hole. Since the base vacuum requirement at the HV chamber where the atomic beam is produced is only of the order of 6×10^{-8} mbar, we have used viton seals to attach the glass windows, broadband AR coated around 780 nm on both sides, to the cuboid chamber using steel cover plates. Viton o-ring seal is used on both sides of the glass windows, resulting in reliable seals which ensured zero breakage of the glass windows.

The cuboid chamber is connected to the UHV chamber through a CF 35 port. A copper rod with a centered hole was inserted in the port between the cuboid and the UHV chamber. The hole size is 2 mm up to a length of 1 cm starting from the 2D cooling chamber and then its size is 3 mm up to a length of 3 cm ending at the UHV chamber side. The copper rod has a 45° cut with respect to the axis on one end and this was hand-polished for 90% reflectivity at the front surface in order to allow an axial light beam inside the cuboid chamber for retardation and Doppler cooling of the atoms in the axial direction. This copper rod with the hole doubles up as a differential pumping separator and a mirror.

We have used a circularly polarized light beam expanded using a pair of cylindrical lenses (horizontal waist size of around 96 mm and vertical waist size of 9 mm) for the transverse cooling and trapping so as to have a large cooling volume. In order to avoid using large $\lambda/4$ plates we have retroreflected the transverse cooling beams using long right-angled prisms with base dimensions 10 cm×2.5 cm (Astro-Optics Industries, Mumbai), where the light gets retroreflected after two total internal reflections, preserving the helicity of the circularly polarized light as required for the magneto-optical trapping. This eliminated the need for independent beams and their independent expansion. This optical design without large or multiple wave plates also reduces the cost significantly.

Cooling in the longitudinal direction reduces the mean velocity and the width of the velocity distribution, and almost all the atoms in the resulting beam have velocity less than the capture velocity of a standard three-dimensional MOT. This enables the efficient loading into a 3D MOT without any further cooling. Moreover, due to longitudinal cooling, the atoms spend more time in the transverse cooling beams, so their transverse velocity and hence divergence are reduced and the beam density is enhanced, increasing the probability of their passing through the small differential pumping hole into the UHV chamber. The divergence of the atomic beam in the UHV chamber is determined by the size of the differential pumping hole and the length of the hole through the copper rod.

A pressure of 4×10^{-8} mbar could be maintained in the 2D cooling chamber using a 20-l/s ion pump. Rubidium metal (in an ampule) is used as the source of rubidium atoms. The glass vial containing the ampule of 5 g Rb was kept in a tube connected to the cuboid chamber through an in-line valve and it was broken in vacuum. The background rubidium pressure in the 2D chamber could be varied by heating the tube containing the ampule as well as by controlling the opening of the inline valve. There were some pieces of graphite rod inserted in the pumping path between the Rb source and the ion pump, to help in reducing the corrosion

inside the ion pump. The UHV vacuum chamber for the 3D MOT and other experiments is maintained at less that 3×10^{-10} mbar with a 75-l/s ion pump. At higher pressures around 3×10^{-7} mbar in the $2D^+$ MOT chamber, the pressure in the 3D MOT UHV chamber could be maintained below 6×10^{-10} mbar (an additional sublimation pump would bring this down below 10^{-10} mbar for BEC experiments).

The cooling laser beam was derived from a 780-nm external cavity diode laser (ECDL: Toptica DL100). We produce beams of ^{85}Rb as well as ^{87}Rb, depending on the experiment. For the ^{85}Rb beam, the laser frequency was 2.2Γ detuned from the $^5S_{1/2,}F=3\rightarrow{}^5P_{3/2,}F=4$ transition. The repumping beam was derived from a 795-nm ECDL and the transition $^5S_{1/2,}F=2\rightarrow{}^5P_{1/2,}F=3$ was used for the repumping. For producing the ^{87}Rb beam, the laser frequency is detuned 2Γ from the $^5S_{1/2,}F=2\rightarrow{}^5P_{3/2,}F=3$ transition. The repumping beam was derived from a 795-nm ECDL and the transition $^5S_{1/2,}F=1\rightarrow{}^5P_{1/2,}F=2$ was used for the repumping. Cooling and repumping laser beams are first independently expanded with telescopes into a circular cross section with waist 9 mm. After mixing the cooling and repumping beams, the circularly polarized beams were expanded along the axis of the 2D cooling chamber using a pair of cylindrical lenses with focal lengths −30 mm and 200 mm. The advantage of large cooling volume is twofold. First, a large number of atoms are captured by the magneto-optical potential and, second, the atoms with higher axial velocities also get sufficient time in the cooling volume to get transversely cooled enough to get transmitted through the hole.

A linearly polarized pushing light beam of the circular cross section with waist 9 mm was aligned along the atomic beam axis towards the UHV chamber. Also a similar retarding light beam was introduced into the chamber from the opposite direction by reflection from the 45° copper mirror as shown in Fig. 1. The hole in the center of the copper mirror produces a shadow at the center of the retarding beam. The pushing and retarding beams provide the longitudinal cooling of the atomic beam, reducing the width of the longitudinal velocity distribution. The imbalance of the radiation pressure of the longitudinal cooling beams on the atoms due to the hole in the retarding beam is used to push the atomic beam through the differential pumping hole into the UHV chamber to load the 3D MOT.

Mild heating of the source chamber with heater tapes to about 50 °C provides enough quantity of rubidium to operate the $2D^+$ MOT and to optimize it. Usually the heating is kept off during operation, with an occasional boost in heating at 40–50 °C lasting a few minutes, and the $2D^+$ MOT beam operates in optimized condition at around a pressure of 3×10^{-7} mbar, close to the room-temperature vapor pressure of rubidium. The transverse magnetic field gradient is produced using two pairs of racetrack coils in anti-Helmholtz configuration. The requirement is to have both the field and field gradient to be zero along the symmetry axis of the chamber. A current of 1.5 A. per coil produces a transverse field gradient of 15 G/cm. The transverse cooling beams were circularly polarized appropriately according to the magnetic field directions. By fine-tuning the currents in the coils independently, the transverse position of the $2D^+$ MOT can be shifted to maximize the flux through the differential pumping hole.

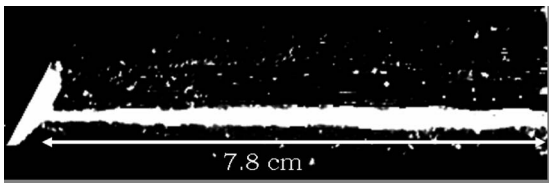

FIG. 2. A fluorescence picture of the atoms in the $2D^+$ MOT in the 2D cooling chamber taken with a charge-coupled-device (CCD) camera when the pushing and the retarding light beam powers are almost balanced (a partial view of the copper reflector is also visible at the left end).

The transverse velocity distribution of the atoms in the cold atomic beam is limited by the differential pumping hole diameter apart from the transverse cooling factors. The atoms with high transverse velocities are filtered out by the 2-mm hole in the differential pumping tube. Hence a well-collimated beam with small transverse temperature can be obtained with small divergence so as to efficiently load a 3D MOT. A fluorescence image of the cold atoms in the $2D^+$ MOT is shown in Fig. 2. The longitudinal velocity distribution of the atoms in the beam is determined by the position at which the atoms enter the cooling volume and hence get decelerated to different extents along the atomic beam axis.

A number of measurements were done to characterize the cold atomic beam. The longitudinal velocity distribution, atomic beam flux, divergence of the atomic beam after the differential pumping hole into the UHV chamber, loading rate into a 3D MOT, dependence of the atomic beam flux on the rubidium vapor pressure, cooling laser power, detuning, and the dimensional extent of the transverse cooling beams, etc., were measured. Most of the measurements presented in this paper were done for ^{85}Rb, though comparisons were made with a ^{87}Rb beam as well, especially the measurements of the atomic beam flux and its dependence on the Rb vapor pressure as well as the measurement of the longitudinal velocity distribution. Since these measurements were then compared with the results from a numerical simulation of the setup, we discuss the numerical simulation first before describing the details of the measurements.

III. DESCRIPTION OF THE NUMERICAL SIMULATION

A numerical simulation was done to model the atomic beam characteristics. This simulation integrates the equation of motion of the atoms captured from the background vapor in the 2D cooling chamber into the atomic beam, which then passes through a hole into the other UHV chamber where the flux is measured.

The initial positions of the atoms are chosen randomly from within the 2D cooling chamber. The initial velocities are chosen according to Maxwell-Boltzmann distribution at 300 K temperature using the Box-Muller transformation [13] and Monte Carlo method [14]. The trajectories of the atoms in the presence of the radiation force **F** due to the laser

beams, in the magnetic field used for the magneto-optical trapping, are integrated using the Runga-Kutta method.

In the simulation, the velocity-dependent force on the atoms was imparted by four transverse cooling laser beams elongated along the longitudinal direction and a pair of longitudinal cooling beams along the atomic beam axis. All the laser beams were chosen to have Gaussian intensity profiles truncated to the size of the AR-coated windows of the chamber along with appropriate polarizations and directions for magneto-optical trapping. The position dependence of the force was incorporated by the quadrupole magnetic field produced by the four rectangular coils given by

$$\mathbf{B} = (gx, -gy, 0), \tag{1}$$

where g is the magnetic field gradient along the transverse (x-y) directions and the field is zero along the z direction which signifies the absence of trapping along the atomic beam axis. Since we used two pairs of coils symmetrically around the cuboid chamber, the gradients in the two directions have the same magnitude.

We have considered a simplified model of the atomic transition utilized for the cooling process as $|g, J_g=0\rangle \leftrightarrow |e, J_e=1\rangle$ since this model works for any $J_g \leftrightarrow J_e=J_g+1$ transition as well. $|g\rangle$ and $|e\rangle$ are the ground state and the excited state, respectively, of the transition. A similar approach has been described in [11].

For the description of the motion of the atoms in a magneto-optical trap [15], we considered the radiative force on the atoms in the low-intensity limit. The total force on the atoms is given by $\mathbf{F}=\mathbf{F}_+ + \mathbf{F}_-$, where

$$\mathbf{F}_\pm = \pm \frac{\hbar \mathbf{k} \Gamma}{2} \frac{S_0}{1 + S_0 + (2\delta_\pm/\Gamma)^2}, \tag{2}$$

Γ is the natural linewidth of the atomic transition, $\hbar = h/2\pi$, where h is Planck's constant, $\mathbf{k}$ is the wave vector of the laser beam, $S_0 = I/I_{sat}$ is the on-resonance saturation parameter for the cooling laser, where I is the intensity of the laser beam used for the atomic transition, and I_{sat} is the saturation intensity for the transition (I_{sat} for the D_2 resonance line in Rb is 1.6 mW/cm^2).

The detuning $\delta_\pm$ for each laser beam is given by

$$\delta_\pm = \delta \mp \mathbf{k} \cdot \mathbf{v} \pm \mu' B/\hbar \, . \tag{3}$$

Here δ is the detuning of the laser beam from the atomic resonance, $\mathbf{v}$ is the velocity of the atoms, $\mu' \equiv (g_e m_e - g_g m_g)\mu_B$ is the effective magnetic moment for the transition used, subscripts g and e refer to ground and excited states, $g_{g,e}$ is the Lande g factor, μ_B is the Bohr magneton, and $m_{g,e}$ is the magnetic quantum number. $B = \sqrt{B_x^2 + B_y^2}$ is the magnitude of the local magnetic field. At the periphery of the cooling volume of the 2D MOT the detuning due to the magnetic Zeeman shift (20–30 MHz) is comparable to the mean value of the Doppler shift as the atoms start to get trapped by the cooling light ($\simeq$30 MHz for atoms with a velocity of about 20 m/s). Though the Doppler term becomes much smaller, of the order of a few MHz, once the atoms are effectively trapped in the 2D MOT and their transverse velocity is reduced below a few m/s, the Zeeman term also becomes negligible since the field decreases towards the symmetry axis of the trap (about a gauss at 1 mm from the symmetry axis). Heating due to spontaneous emission is neglected in the simulation since its effect on the atomic motion is much smaller than the radiation pressure force. Also we neglect the small dipole force on the atoms due to the gradients in the light intensity.

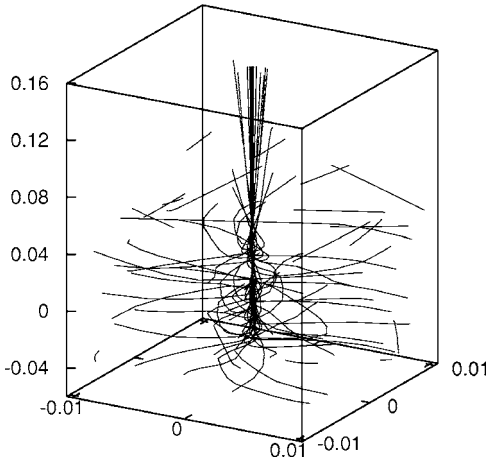

FIG. 3. Simulated trajectories of 100 atoms captured in the 2D$^+$ MOT and transferred to the atomic beam (lengths in meters).

One of the longitudinal cooling beams propagating towards the atomic beam direction (+z direction) was truncated according to the hole size of 2 mm as it reaches the hole meant for the passage of the atomic beam. Also the intensity of the retarding beam traveling in the $-z$ direction was put to zero along the cylindrical region of diameter 2 mm at its center so as to create a radiation imbalance in that region simulating the shadow at the center of the retarding beam.

Starting with an initial sample of 5×10^4 atoms, we have computed their individual trajectories and obtained the fraction of atoms being captured and transferred into the atomic beam. To calculate the atomic beam flux, the initial atom number was scaled up according to the rubidium vapor pressure in the 2D cooling chamber. We have also simulated our various measurements of the atomic beam characteristics like the variation of the atomic beam flux with the rubidium vapor pressure, cooling beam power, and the transverse cooling beam length. The trajectories of 100 atoms calculated by 3D numerical simulation are shown in Fig. 3.

Since we have studied the variation of the atomic beam flux with Rb vapor pressure up to 1.5×10^{-6} mbar, we have also taken into account the effect of collisional losses which become significant at pressures above 3×10^{-7} mbar in a 2D$^+$ MOT where the time scale for collisions of atoms in the beam with the background gas becomes smaller than the time spent by the atoms in the beam until they reach the differential pumping hole. The collisional losses from the atomic beam due to collisions with the background rubidium atoms and cold collisions between the atoms in the cold atomic beam are accounted for by an exponential factor [16]. Hence the atomic beam flux ϕ is given as

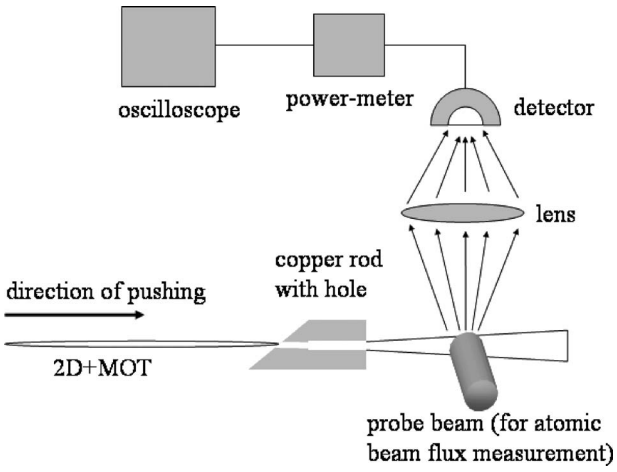

FIG. 4. The schematic diagram of the experimental arrangement to characterize the cold atomic beam in the UHV chamber.

$$\phi = \phi_0 \exp\left[-\left(\Gamma_{coll} + \beta \int n^2(\mathbf{r}) d^3 r \right) \langle t_a \rangle \right], \qquad (4)$$

where ϕ_0 is the simulated atomic beam flux without considering the collisional losses. $\Gamma_{coll}=n_{Rb}\sigma_{eff}\langle v\rangle$ is the collisional loss rate due to collisions of the atoms in the beam with the background rubidium atoms, $\langle t_a\rangle$ is the average time the atoms spend in the beam, $n(\mathbf{r})$ is the position-dependent atomic density in the beam, and β is the two-body loss rate coefficient which describes the cold collisions between the atoms in the cold atomic beam. n_{Rb} is the thermal rubidium atom number density, σ_{eff} is the effective collision cross section, and $\langle v\rangle$ is the mean velocity of the thermal rubidium atoms. We have neglected the three-body collisional losses which are significant only at much higher densities (e.g., in tight magnetic traps or BEC) as compared to the densities obtained in a MOT.

IV. MEASUREMENTS OF ATOMIC BEAM PROPERTIES

Both the atomic beam flux and velocity were measured using fluorescence detection of the atomic beam in the UHV chamber.

To measure the flux of the atomic beam, a 300-μw retroreflected probe beam with circular cross section and waist 1 cm was aligned orthogonal to the atomic beam, inside the UHV chamber, and the laser frequency was swept across the resonance. The resonance fluorescence signal from the atoms in the atomic beam passing through the probe beam was detected using a large-area Si detector connected to a calibrated power meter (Newport Model 1835-C). The schematic diagram of the experimental setup for the atomic beam flux measurement is shown in Fig. 4. Usually, the atomic beam flux is optimized before the measurement by adjusting the position of the line of zero magnetic field by adjusting the current in the individual coils so as to ensure the passage of the atomic beam through the differential pumping hole with minimum geometric losses.

Though it is possible to obtain significant increase in the S/N ratio in the detection signal using phase-sensitive techniques, as we demonstrated recently with the time-of-fight (TOF) signals of probe absorption [17], the signal obtained from the high flux beam is large enough to be detected with high S/N using only a high-pass filter.

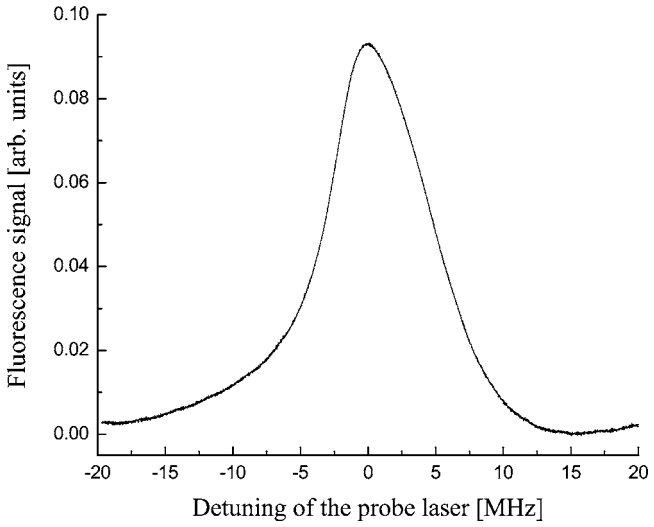

FIG. 5. A typical fluorescence signal obtained in the experiment sketched in Fig. 4, from which the instantaneous number of atoms in the atomic beam from the $2D^+$ MOT is determined.

From the fluorescence signal, the instantaneous number of atoms at the probe volume is determined. Knowing the probe volume and the mean velocity of the atoms, the atomic beam flux is calculated according to Eq. (7). A typical fluorescence signal used for the determination of the atomic beam flux in a $2D^+$ MOT is shown in Fig. 5.

To measure the mean longitudinal velocity and the velocity distribution of the atomic beam, the circular probe beam of 1 cm waist was aligned through the atomic beam at 45° with respect to the atomic beam axis and retroreflected. The laser frequency was swept across the resonance, and the fluorescence signal was detected. The experimental arrangement is shown in Fig. 6.

A photon with wave vector $\mathbf{k}$ appears to have a frequency

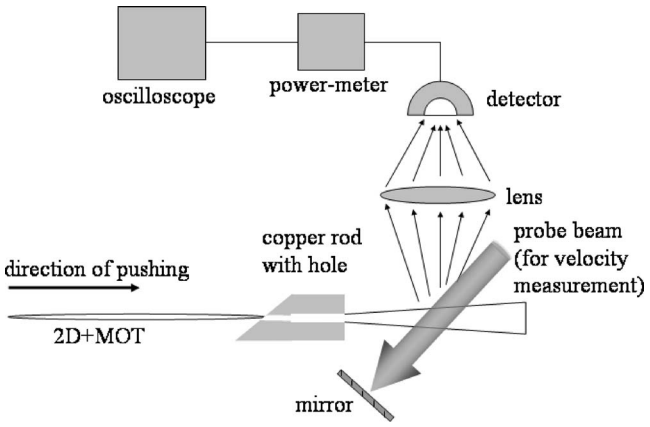

FIG. 6. The schematic diagram of the experimental arrangement to determine the longitudinal velocity of the atoms in the cold atomic beam.

$$\omega' = \omega - \mathbf{k} \cdot \mathbf{v} \tag{5}$$

to an atom moving with velocity **v**. Hence, the mean longitudinal velocity is given by

$$\langle v_z \rangle = \frac{\Delta \nu_d \lambda}{\cos \theta}, \tag{6}$$

where λ is the probe laser wavelength and $\Delta \nu_d$ is the Doppler shift, measured from the relative frequency shift between the fluorescence spectra from the probe beam aligned at an angle θ with respect the atomic beam direction and the probe beam aligned orthogonal to the atomic beam direction.

From the shift of the peak of the Doppler profile from the resonance frequency, the longitudinal velocity of the atoms in the atomic beam can be calculated taking into account the 45° angle between the atomic beam and the direction of the probe laser beam. The longitudinal velocity distribution can be determined from the width of the Doppler profile after deconvolution of the contribution of the natural linewidth of the atomic transition to the width of the signal.

The atomic beam flux ϕ can be calculated as

$$\phi = \frac{4\pi S_d \langle v_z \rangle}{d\Omega L_p R_{sc} h \nu}. \tag{7}$$

Here, S_d is the signal at the detector due to the fluorescence signal from the atomic beam (when the probe laser is resonant), $d\Omega$ is the collection solid angle of the detector, $\langle v_z \rangle$ is the mean longitudinal velocity of the atomic beam, L_p is the diameter of the probe beam aligned orthogonal to the atomic beam axis, h is the Planck's constant, ν is the rubidium D_2 transition frequency, and R_{sc} is the rate of photon scattering by individual atoms where R_{sc} is given by

$$R_{sc} = \frac{\Gamma S_o}{2(1 + S_o)}. \tag{8}$$

where Γ is the natural linewidth of the rubidium D_2 resonance line and S_o is the on-resonance saturation parameter for the probe laser.

The dependence of the atomic beam flux and its velocity characteristics on the detuning of the cooling laser was also investigated. Such a study was done for the case of the detuning of the pushing laser beam for a slow atomic beam produced from a 3D MOT by Wohlleben *et al.* [11]. In our case the 2D cooling laser beams and the pushing and retarding laser beams are all derived from the same laser, and the experimental situation is different from, and in fact simpler than, the one in [11]. We see a critical dependence of the flux on the detuning of the laser, though the region of stable high-flux operation extends over about 3 MHz, allowing good stability.

To determine the divergence of the atomic beam produced by the $2D^+$ MOT, the variation of the fluorescence signal from the atomic beam with the resonant probe beam aligned perpendicular to the atomic beam axis was studied as a function of the size of the probe beam. This gave the measure of the width of the atomic beam at the position of the probe (7.5 cm away from the 3-mm hole in the copper rod). The divergence was determined with respect to the 3-mm hole through which the atomic beam enters the UHV chamber since the hole limits the initial divergence of the atomic beam in the UHV chamber.

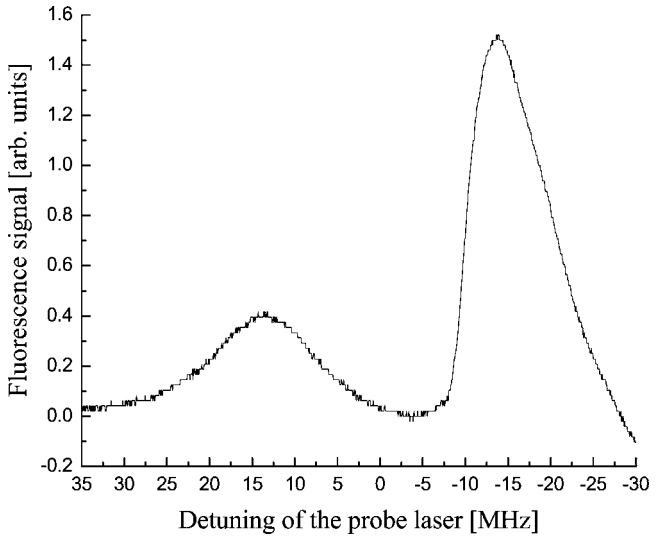

FIG. 7. A typical fluorescence signal obtained in the experiments shown in Fig. 6. The velocity distribution of the atoms in the $2D^+$ MOT beam is estimated from this signal.

V. RESULTS AND DISCUSSION

A typical fluorescence signal, as the laser frequency is scanned over several MHz across the resonance from blue-detuning to red-detuning of the laser with respect to the $^5S_{1/2,}\ F=3 \rightarrow {}^5S_{3/2,}\ F=4$ transition of ^{85}Rb, for the measurement of the atomic beam velocity (schematic shown in Fig. 6) of the $2D^+$ MOT is shown in Fig. 7. The corresponding fluorescence signal for the pure 2D MOT (when the laser beams along the longitudinal direction are blocked) is shown in Fig. 8. Two peaks are observed in the fluorescence signals

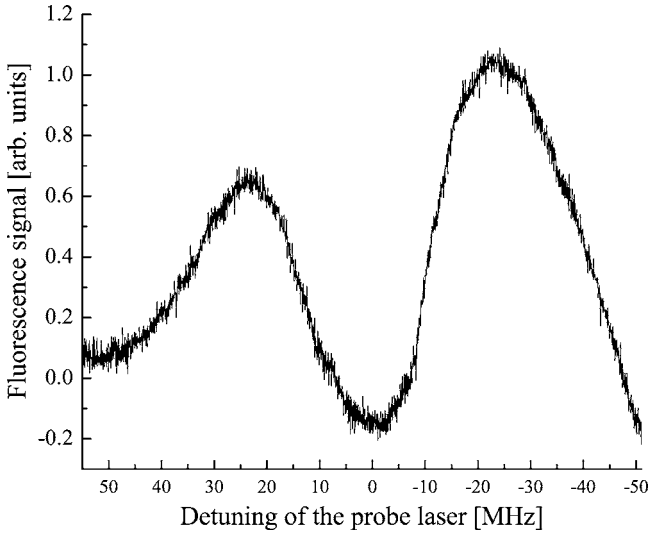

FIG. 8. A typical fluorescence signal for the determination of the atomic beam velocity distribution in the case of a pure 2D MOT.

in Figs. 7 and 8. The peaks occur symmetrically on both sides of the resonance laser frequency. The resonance frequency is determined by calibrating the frequency scale with respect to the saturation absorption spectroscopy signal.

The peak at the left is caused predominantly by the interaction of the atoms with the retroreflected part of the probe beam which travel towards ($\mathbf{k}\cdot\mathbf{v}$ positive) the direction of propagation of the atomic beam, making an angle of 45° with respect to the atomic beam axis. During the start of the scan this beam is blue-detuned with respect to the resonance, but the Doppler shift towards red brings it closer to the resonance. As the retroreflected beam scans over the resonance, the input probe beam for which $\mathbf{k}\cdot\mathbf{v}$ is negative is far-detuned to the blue. This peak is relatively broader than the other peak on the right due to two reasons: (a) The radiation pressure has a large component along the direction of motion of the atoms near resonance, and this pushes the atoms out of the probe beam. (b) It occurs at frequencies of the input probe beam that are blue-detuned to the resonance frequency and hence no further Doppler cooling happens in the probing region.

The other peak at the right is predominantly due to the interaction of the atoms with the input probe beam that is counterpropagating at 45° with respect to the atomic beam axis, with $\mathbf{k}\cdot\mathbf{v}$ negative. In this case, the radiation pressure helps to decelerate the atoms. This peak is narrower and larger because it occurs when the frequency of the retroreflected beam is red-detuned to the resonance frequency which enables Doppler cooling that causes the atoms to stay for a longer time in the probe beam, enhancing the fluorescence signal. This particular effect is less in the case of the detection of atoms from 2D MOT (Fig. 8) because the atoms from 2D MOT already have a larger longitudinal velocity and hence they spent too small a time in the probe for sufficient cooling to happen. From the shift of the peaks from the resonance, the Doppler shift due to the longitudinal velocity of the atomic beam was determined taking into account the 45° angle that the probe beam makes with the atomic beam axis. From the average width of the fluorescence peaks in Figs. 7 and 8., the width of the longitudinal velocity distribution of the atoms in the atomic beam was estimated for the $2D^+$ MOT and 2D MOT, respectively, after deconvolution of the natural linewidth of the atomic transition.

In the case of the ^{85}Rb $2D^+$ MOT, a mean longitudinal velocity of 15 m/s was measured and the width of the velocity distribution was measured to be 3.5 m/s. The corresponding mean longitudinal velocity in the case of ^{87}Rb was measured to be 17 m/s and the width of the velocity distribution was measured to be 5 m/s. The peak atomic beam flux of 2×10^{10} atoms/s is routinely obtained at the typical room-temperature vapor pressure of rubidium. We have been able to observe up to 3×10^{10} atoms/s in the atomic beam by optimizing the transverse size of the $2D^+$ MOT to fill the differential pumping hole by tuning the 2D quadrupole field gradient. The divergence of the atomic beam produced from the $2D^+$ MOT was measured to be ~26 mrad. The mean longitudinal velocity and the width of the longitudinal velocity distribution of the ^{85}Rb pure 2D MOT was measured to be 26 m/s and 11 m/s, respectively. The mean longitudinal velocity and the width of the velocity distribution is larger in the case of the pure 2D MOT as compared in the $2D^+$ MOT since longitudinal cooling is absent in the 2D MOT.

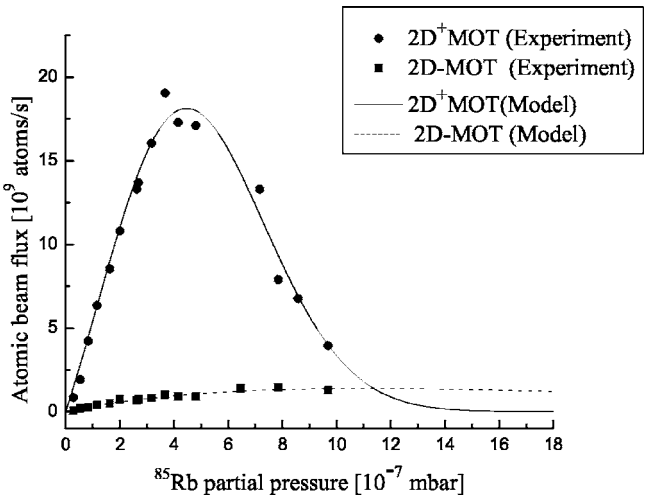

FIG. 9. The variation of the ^{85}Rb atomic beam flux in a $2D^+$ MOT and 2D MOT with the rubidium vapor pressure in beam chamber. The points show the experimental results, and the solid and dashed lines show the prediction of the model for collisional losses from the atomic beam from the $2D^+$ MOT and 2D MOT, respectively. The model for the $2D^+$ MOT takes into account the effect of collisions of the cold atoms in the beam with the hot background atoms as well as the cold collisions between the atoms in the cold atomic beam. The model for the 2D MOT flux takes into account only the collisions of the atoms in the atomic beam with the background atoms since cold collisions are negligible in this case.

The variation of the atomic beam flux was studied as a function of the rubidium vapor pressure in the 2D cooling chamber. The experimental data and the prediction of the model for collisional losses from the atomic beam are shown in Fig. 9. The vapor pressure of rubidium in the 2D cooling chamber was measured using absorption measurements of a laser beam passing through the chamber as the laser frequency was swept across resonance. The calibration of the measurements of the vapor pressure was done by comparison with the absorption measurement in a standard rubidium vapor cell having rubidium vapor pressure of 2.5×10^{-7} mbar at room temperature. For data taken at high Rb vapor pressures, the measured contribution of the thermal atoms to the fluorescence amounts to a maximum of around 35% at 9×10^{-7} mbar whereas it is less than 3% of the peak signal around 3×10^{-7} mbar. The fluorescence was subtracted to determine the actual value of the cold atomic beam flux.

At lower pressures ($<10^{-7}$ mbar), the flux increases linearly with the pressure. The decrease in flux at higher rubidium vapor pressure in the $2D^+$ MOT, as shown in Figs. 9 and 10, is due to the increase in the collision rate with hot background atoms as well as due to the cold collisions among the atoms in the cold atomic beam as given in Eq. (4). The collision between cold atoms in the atomic beam and the background atoms is mainly due to the long-range resonant dipole-dipole interaction [18] described by the potential of the form C_3/R^3, between a ground-state atom and an excited-state atom in the presence of near-resonant light, where R is the interatomic separation and $C_3\approx5.65\times10^{-48}$ Jm^3 for ru-

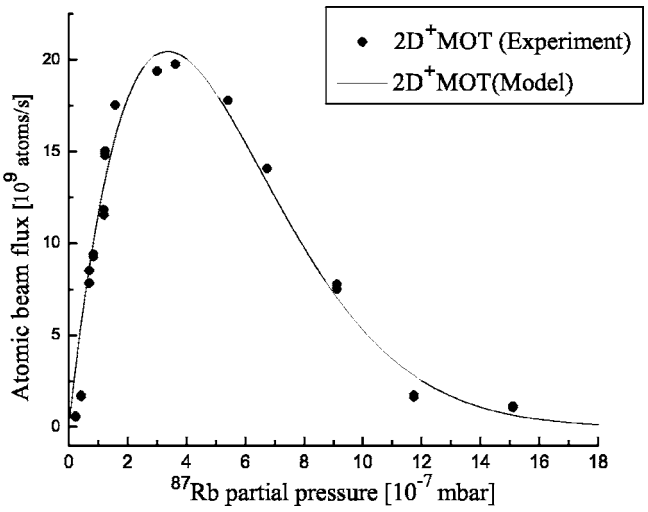

FIG. 10. The variation of the ^{87}Rb atomic beam flux from the $2D^+$ MOT with the rubidium vapor pressure in the beam chamber. The points show the experimental results, and the solid line shows the prediction from the model for collisional losses from the atomic beam.

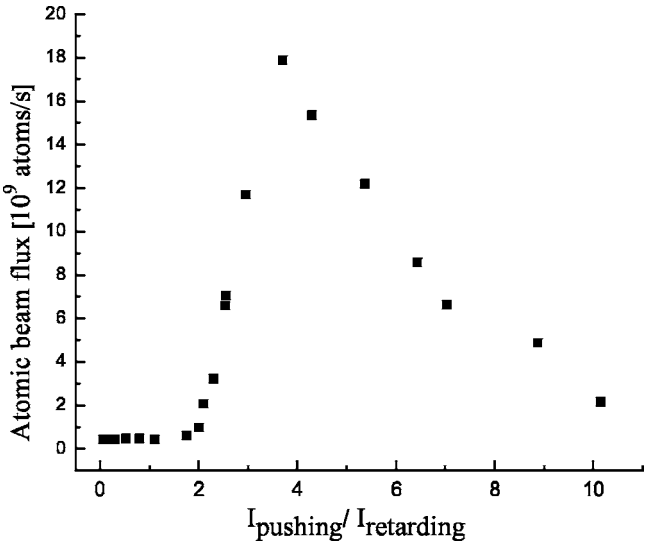

FIG. 11. Experimental data showing the variation of the ^{85}Rb atomic beam flux in the $2D^+$ MOT with power balance between the pushing and retarding beams.

bidium (D_2 transition). The effective collisional cross section σ_{eff} in this approximation is given by [18]

$$\sigma_{eff} = \pi\left(\frac{f(3)C_3}{mv_{esc}v}\right)^{2/3}, \tag{9}$$

where $f(3)=4$, m is the mass of a ^{85}Rb atom, v_{esc} is the escape velocity of the atoms from the trap, and v is the velocity of the background ^{85}Rb atoms. The calculated value of σ_{eff} for ^{85}Rb from Eq. (9) considering parameters for $2D^+$ MOT is 1.2×10^{-12} cm^2. By fitting Eq. (4) to the experimental data of the $2D^+$ MOT as shown in Fig. 9, the value of the effective collision cross section for loss out of the ^{85}Rb beam due to collision with the background atoms is determined as $\sigma_{eff}=0.81\times10^{-12}$ cm^2. The corresponding effective collision cross section for ^{87}Rb (Fig. 10) is determined as $\sigma_{eff}=1.43\times10^{-12}$ cm^2. The statistical error of the value of σ_{eff} obtained from the fit to the experimental data is about 15%.

In the case of the 2D MOT of ^{85}Rb, Eq. (4) was fitted to the data (Fig. 9) without the second term for cold collisions in the exponential factor. The model for the 2D MOT flux takes into account only the collisions of the atoms in the atomic beam with the background atoms since the cold collisions are negligible at the lower atomic density and the higher longitudinal velocity in the 2D MOT as compared to the situation in the $2D^+$ MOT. The effective collision cross section from the fit to the experimental data for the 2D MOT was determined to be $\sigma_{eff}=0.9\times10^{-12}$ cm^2.

The position-dependent atomic density $n(\mathbf{r})$ in the atomic beam was determined from the intensity profile of the fluorescence from the atomic beam in the image taken by a CCD camera. By fitting Eq. (4) to the experimental data, the value of the two-body loss coefficient β for ^{87}Rb was determined as $\beta=6.6\times10^{-16}$ cm^3/s. The corresponding value of β for ^{85}Rb is determined to be 7×10^{-15} cm^3/s. These values of β are orders of magnitude lower than the typical values in a 3D MOT [16] because in the atomic beam, the density of the cold atoms (10^8 atoms/cm^3) is much lower compared to that in the 3D MOT (10^{11} atoms/cm^3) which has larger confinement. The measured value of β for ^{85}Rb is larger than that of ^{87}Rb which is consistent considering that the hyperfine-changing collisions [16,19] are larger in the case of ^{85}Rb. This can be attributed to the smaller (3 GHz) hyperfine splitting between the ground states [20] in ^{85}Rb. The value of β depends on the intensity of the trap laser as well as on its detuning. The statistical error of the value of β obtained from the fit to the experimental data is about 30%.

The atomic beam flux from the 2D MOT is considerably lower as compared to the flux from the $2D^+$ MOT as shown in Fig. 9. This of course has been seen in earlier implementations of similar systems [8]. Due to the absence of longitudinal cooling in the 2D MOT, atoms spend relatively smaller durations in the transverse cooling beams, resulting in larger transverse velocities. Hence they get filtered out by the differential pumping hole, resulting in the lower flux compared to the flux from the $2D^+$ MOT. Due to the higher velocity of the atoms in the 2D MOT, the atomic beam flux is not affected much by collisions when the rubidium vapor pressure is increased. This is evident in the experimental data as well as in the prediction of the theoretical model presented in Eq. (4) and shown in Fig. 9.

The atomic beam flux from the $2D^+$ MOT was studied as a function of the relative intensities of the pushing and retarding beams along the atomic beam axis as shown in Fig. 11, since this ratio is an important parameter for optimizing the atomic beam flux. At high ratios of the intensities of the pushing and retarding beams, the atomic beam flux decreases as the molasses cooling in the longitudinal direction becomes inefficient. Therefore, the atoms do not spend enough time in the transverse cooling beams and, as a consequence, the transverse cooling also becomes inefficient. As the power ratio between the pushing and retarding beams is changed from minimum to maximum, the mean longitudinal velocity

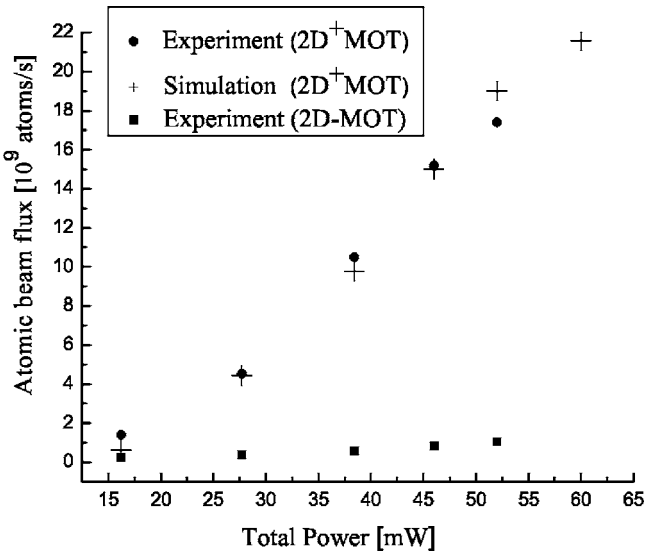

FIG. 12. Experimental and simulation data showing the dependence of the ^{85}Rb atomic beam flux of the 2D$^+$ MOT on total laser power. Also experimental data for flux variation with total laser power in the 2D MOT are shown for comparison.

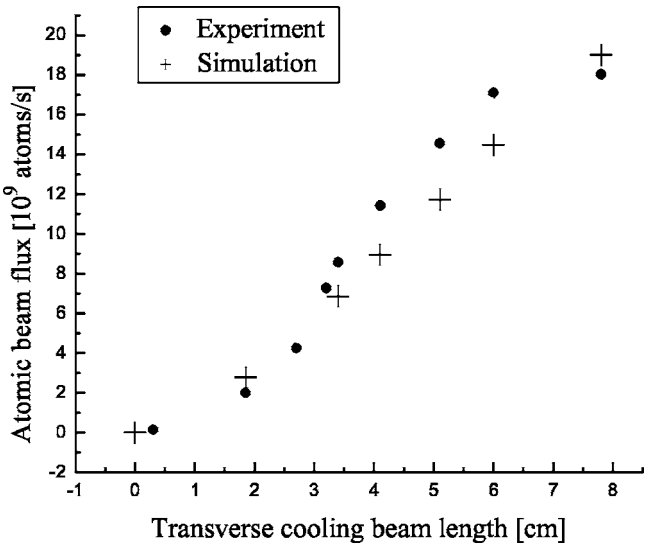

FIG. 13. Experimental and simulation data showing the variation of the ^{85}Rb atomic beam flux in the 2D$^+$ MOT with the length of the transverse cooling beam.

of the atoms in the beam changes by only 10%.

The flux of the atomic beam produced in the 2D$^+$ MOT and in the 2D MOT was studied with respect to the variation of the total laser power used to produce the atomic beam. The results are shown in Fig. 12. The power in the transverse beams is about 80% of the total power. The atomic beam flux increases almost linearly with the increasing intensity of the cooling laser. This can be explained heuristically by considering that higher intensities cause power broadening of the atomic spectral lines and hence enable atoms with higher velocities to get captured in the atomic beam, resulting in an increase of the atomic beam flux. Also, at higher intensities, the magneto-optical potential becomes steeper, resulting in more compression of the atomic beam which increases the probability of passage of the atoms in the atomic beam through the hole. The simulated atomic beam flux as a function of total cooling laser power matches well with the experimental data.

The variation of the atomic beam flux was studied as a function of the length of the cross section of the transverse cooling laser beam. The transverse size of the expanded laser beam is changed by blocking progressively the beam from the end farther from the differential pumping hole. Thus the total power in the cooling beams reduces as the transverse beam size is reduced. The experimental data points and the results from the numerical simulation are shown in Fig. 13. The atomic beam flux increases with the transverse size of the cooling beams since the atoms with higher longitudinal velocities also get captured in the atomic beam as their transverse velocity is reduced due to the efficient cooling over the longer duration they interact with the cooling light. It is remarkable that with a transverse cooling length of only 3 cm and a total cooling laser power less than 30 mW, the flux is as high as 5×10^9 atoms/s, all of which can be captured into a 3D MOT. These data reiterate that such a compact 2D$^+$ MOT beam setup is the ideal source of high flux of cold atoms for experiments in Bose-Einstein condensation, atom interferometry, and atom optics, especially for transportable systems as needed in atom gravimeters and inertial sensors.

The variation of the atomic beam flux with the detuning of the cooling and pushing and retarding beams was studied for the ^{87}Rb beam. The experimental data are shown in Fig. 14. Since the detuning of the pushing beam affects also the average velocity of the beam, we measured the change in the average velocity of the beam by monitoring the Doppler shift of the spectral line with the probe beam crossing the atomic beam at a 45° angle. The change in the average velocity is limited to about 35% when the detuning is changed by 2Γ, as shown in Fig. 15, and the atomic beam flux data shown in Fig. 14 are corrected for this change.

In order to optimize the atomic beam flux through the hole separating the 2D cooling chamber and the main UHV chamber, it is to be ensured that the transverse cooling beams

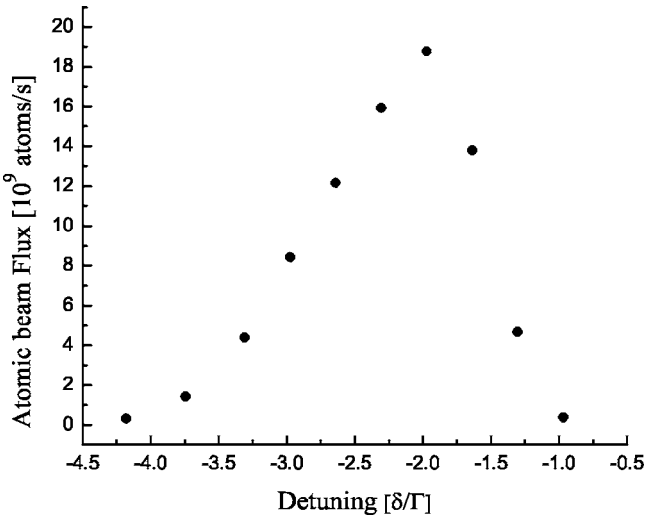

FIG. 14. Experimental data showing the variation of the ^{87}Rb atomic beam flux from the 2D$^+$ MOT with cooling beam detuning.

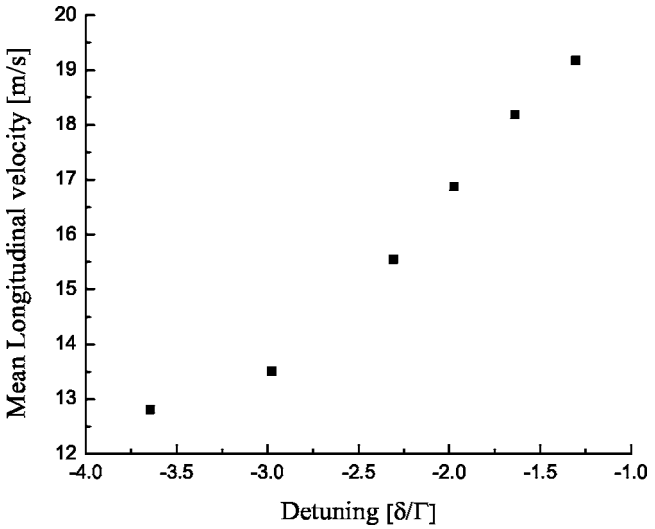

FIG. 15. Experimental data showing the variation of the mean longitudinal velocity of the ^{87}Rb atomic beam from the $2D^+$ MOT with detuning of the cooling laser.

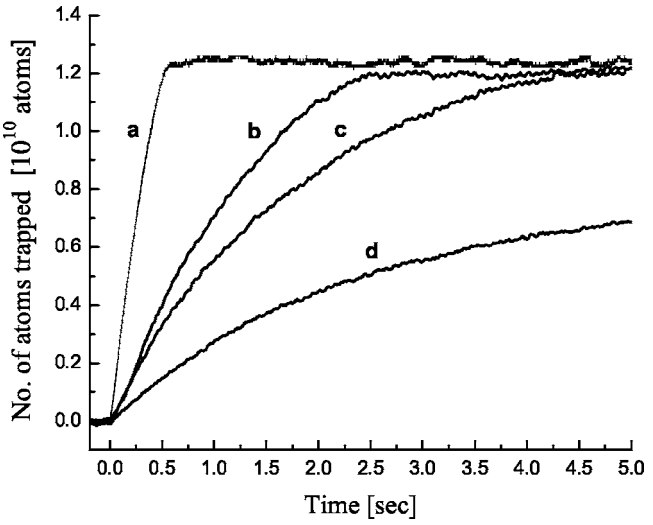

FIG. 16. Variation of the fluorescence from the MOT with time depicting the loading of ^{87}Rb atoms from the $2D^+$ MOT atomic beam into the 3D MOT. The various loading curves correspond to the loading of atoms for different atomic beam fluxes. (*a*) Ultrafast loading of the 3D MOT from the atomic beam with a flux ϕ of about 2.7×10^{10} atoms/s; the time constant τ is 0.29 s. 3D MOT loading with atomic beams having lower values of flux is shown for comparison. (*b*) $\phi\simeq7\times10^9$ atoms/s, $\tau=1.1$ s, (*c*) $\phi\simeq4.7\times10^9$ atoms/s, $\tau=1.6$ s, and (*d*) $\phi\simeq2\times10^9$ atoms/s, $\tau=2.7$ s. For curves *c* and *d*, τ is estimated from an exponential growth function fit; for curves *a* and *b*, τ is defined as the time taken to reach $(1-1/e)$ of the saturation limit. In the absence of saturation, the atom number would have reached asymptotically to 2.7×10^{10} with a time constant of 0.845 s in the case of curve *a*, for example.

are correctly balanced near the hole. Otherwise the strong unbalanced radiation pressure can deflect away the cooled atoms in the beam from the beam axis before they enter the hole, thus reducing the overall beam flux. In our design with the 45° copper mirror, the beam intensities have to be carefully balanced for the pushing and retarding beams as well, and this is easily done by control with a wave plate and a polarizing beam splitter.

VI. LOADING OF ATOMS IN A 3D MOT

The atoms from the $2D^+$ MOT cold atomic beam were loaded into a 3D magneto-optical trap to form a large MOT with an atom number up to 1.2×10^{10} atoms. The high flux of atoms in the beam produced by the $2D^+$ MOT with their velocity smaller than the capture velocity of a 3D MOT results in ultrafast loading of the MOT with high number density (the rubidium cloud is easily visible to the naked eye and can be imaged in color on a digital still camera) [21]. Within 500 ms, 1.2×10^{10} atoms are loaded into a 3D MOT of size ~5 mm as measured from the fluorescence collected in the calibrated detector, plotted in Fig. 16. This loading rate is about 100 times faster compared to what is typically possible in the double-MOT systems, where usually the second MOT is loaded to less than 10^9 atoms after many pulsed transfers of atoms over several seconds from the first MOT which is operated at a high partial pressure. Since the lifetimes of the final trap in the double-MOT system and in the beam-loaded MOT are similar, it is a significant advantage to reduce the atom loading time for subsequent experiments—e.g., to proceed to produce BEC by evaporative cooling. The loading rate reduces by a factor of 10 when the axial beams were blocked—i.e., when the loading was done from a 2D MOT. Surprisingly, we observe a flux of about 1×10^8 atoms/s in the cold atomic beam even in absence of the 2D quadrupole magnetic field in which case there is only a $2D^+$ molasses at 2Γ detuning in the source chamber. This shows that even a simple $2D^+$ molasses source of cold atoms is as effective as a conventional double-MOT arrangement for preparing UHV MOT's.

The fast loading saturates the trap in 0.5 s as seen in the abrupt change of slope in the increase of the fluorescence in Fig. 16. Since the decay time constant of the trap is about 10 times larger, it is clear that the loading stops due to the limitations in maximum density imposed by rescattering of photons and light-assisted collisions. The average atom number density obtained is $\sim1.5\times10^{11}$ atoms/cm^3. This is at the limit of the atom number density possible in standard magneto-optical trapping schemes [15] without dark-spot trapping [20,22]. The density limiting factors are mainly the repulsive force due to the reabsorption of emitted photons from some trapped atoms by other atoms in the trap [23,24], cold collisions [16,25,26], and light-assisted collisional losses [20]. Since the size of the atomic cloud also increases as the loading progresses, the maximum density is reached for a smaller number of atoms (10^8) and a smaller size (1 mm) in a time scale of less than 10 ms, and this is essentially the time required to load the trap in experiments progressing towards optical molasses and evaporating cooling to BEC in a far-detuned dipole trap. For evaporative cooling in deeper magnetic traps, it is advantageous to load more atoms and the loading characteristics in our setup approaches what is ideally possible in such experiments.

VII. CONCLUSIONS

A $2D^+$ MOT source of a high-flux cold atomic beam of rubidium was implemented and characterized in detail. Use of relatively small laser power, simple and reliable vacuum design and assembly, and simple optical configuration for the 2D cooling are some of the aspects of the design. Ultrafast saturation loading of about 1.2×10^{10} precooled atoms from this intense beam into a 3D MOT in about 500 ms is demonstrated. The properties of the cold atomic beam are characterized from a number of measurements, and the results are compared with a numerical simulation. Apart from its use as a high-efficiency source of cold atoms for 3D MOT's to proceed towards BEC, the beam is also useful for precision measurements and other experiments where an intense atomic beam with narrow divergence, low mean velocity, and low velocity dispersion are desired.

ACKNOWLEDGMENTS

We thank P. G. Rodrigues and S. Guram for technical support. We thank A. K. Mohapatra and Franck Pereira Dos Santos for helpful discussions. The work of S.C. and S.R. has received partial support from the TIFR Endowment Fund. The experiments are partially funded by the Department of Science and Technology, Government of India.

[1] C. S. Adams, M. Seigel, and J. Mlynek, Phys. Rep. **240**, 143 (1994).
[2] J. Arlt, G. Birkl, E. M. Rasel, and W. Ertmer, Adv. At., Mol., Opt. Phys. **50**, 55 (2005).
[3] R. J. Thompson, G. Rempe, and H. J. Kimble, Phys. Rev. Lett. **68**, 1132 (1992).
[4] T. Lahaye, J. M. Vogels, K. J. Gunter, Z. Wang, J. Dalibard, and D. Guery-Odelin, Phys. Rev. Lett. **93**, 093003 (2004).
[5] William D. Phillips and Harold Metcalf, Phys. Rev. Lett. **48**, 596 (1982).
[6] Z. T. Lu, K. L. Corwin, M. J. Renn, M. H. Anderson, E. A. Cornell, and C. E. Wieman, Phys. Rev. Lett. **77**, 3331 (1996).
[7] J. Schoser, A. Batär, R. Löw, V. Schweikhard, A. Grabowski, Yu. B. Ovchinnikov, and T. Pfau, Phys. Rev. A **66**, 023410 (2002).
[8] K. Dieckmann, R. J. C. Spreeuw, M. Weidemuller, and J. T. M. Walraven, Phys. Rev. A **58**, 3891 (1998).
[9] R. S. Conroy, Y. Xiao, M. Vengalattore, W. Rooijakkers, and M. Prentiss, Opt. Commun. **226**, 259 (2003).
[10] P. Cren, C. F. Roos, A. Aclan, J. Dalibard, and D. Guery-Odelin, Eur. Phys. J. D **20**, 107 (2002).
[11] W. Wohlleben, F. Chevy, K. Madison, and J. Dalibard, Eur. Phys. J. D **15**, 237 (2001).
[12] James M. Kohel, Jaime Ramirez-Serrano, Robert J. Thompson, Lute Maleki, Joshua L. Bliss, and Kenneth G. Libbrecht, J. Opt. Soc. Am. B **20**, 1161 (2003).
[13] G. E. P. Box and Mervin E. Mullar, Ann. Math. Stat. **29**, 610 (1958).
[14] F. James, Rep. Prog. Phys. **43**, 1145 (1980).
[15] Harold J. Metcalf and Peter van der Straten, *Laser Cooling and Trapping* (Springer, Berlin, 1999).
[16] Reńee C. Nesnidal and Thad G. Walker, Phys. Rev. A **62**, 030701(R) (2000).
[17] A. K. Mohapatra and C. S. Unnikrishnan, Pramana, J. Phys. **66**, 1027 (2006).
[18] A. M. Steane, M. Chowdhury, and C. J. Foot, J. Opt. Soc. Am. B **9**, 2142 (1992).
[19] D. Sesko, T. Walker, C. Monroe, A. Gallagher, and C. Wieman, Phys. Rev. Lett. **63**, 961 (1989).
[20] M. H. Anderson, W. Petrich, J. R. Ensher, and E. A. Cornell, Phys. Rev. A **50**, R3597 (1994).
[21] A true color picture of the Rb MOT as visible to the eye, taken using a digital still camera is available at www.tifr.res.in/~filab
[22] Wolfgang Ketterle, Kendall B. Davis, Michael A. Joffe, Alex Martin, and David E. Pritchard, Phys. Rev. Lett. **70**, 2253 (1993).
[23] T. Walker, D. Sesko, and C. Wieman, Phys. Rev. Lett. **64**, 408 (1990).
[24] D. W. Sesko, T. G. Walker, and C. E. Wieman, J. Opt. Soc. Am. B **8**, 946 (1991).
[25] John Weiner, Vanderlei S. Bagnato, Sergio Zilio, and Paul S. Julienne, Rev. Mod. Phys. **71**, 1 (1999).
[26] P. S. Julienne and Jacques Vigué, Phys. Rev. A **44**, 4464 (1991).